

# Gravity-constrained point cloud registration

Vladimír Kubelka, Maxime Vaidis and François Pomerleau<sup>1</sup>

**Abstract**—Visual and lidar Simultaneous Localization and Mapping (SLAM) algorithms benefit from the Inertial Measurement Unit (IMU) modality. The high-rate inertial data complement the other lower-rate modalities. Moreover, in the absence of constant acceleration, the gravity vector makes two attitude angles out of three observable in the global coordinate frame. In visual odometry, this is already being used to reduce the 6-Degrees Of Freedom (DOF) pose estimation problem to 4-DOF. In lidar SLAM, the gravity measurements are often used as a penalty in the back-end global map optimization to prevent map deformations. In this work, we propose an Iterative Closest Point (ICP)-based front-end which exploits the observable DOF and provides pose estimates aligned with the gravity vector. We believe that this front-end has the potential to support the loop closure identification, thus speeding up convergences of global map optimizations. The presented approach has been extensively tested in large-scale outdoor environments as well as in the Subterranean Challenge organized by Defense Advanced Research Projects Agency (DARPA). We show that it can reduce the localization drift by 30 % when compared to the standard 6-DOF ICP. Moreover, the code is readily available to the community as a part of the libpointmatcher library.

## I. INTRODUCTION

Among the Simultaneous Localization and Mapping (SLAM) approaches for mobile robots, cameras and Light Detection And Ranging (lidar) modalities are still the dominant front-end choices [1]. Modern visual SLAM and visual odometry solutions benefit from the complementary nature of Inertial Measurement Unit (IMU) modalities, which provide high-rate linear acceleration and rotational velocity between captured camera frames [2]. Moreover, the acceleration sensed by IMUs allows the detection of the gravity vector. This vector can be used to observe two attitude angles out of three in a global coordinate frame, thus reducing the visual odometry pose estimation problem from 6-Degrees Of Freedom (DOF) to 4-DOF [3]. Similarly, in the domain of lidar SLAM, using IMUs is beneficial for precise point cloud alignment [4]. The two observable attitude angles are often used as penalties in SLAM back-ends during the global map optimization step. These penalties have the benefit of aligning the map with the gravity vector [5]–[7]. This technique reduces map deformations, especially in large environments with a limited number of possible loop closures, such as in underground mines [5]. We will refer to the use of gravity vector in a SLAM back-end as a loosely-coupled solution.

<sup>\*</sup>This research was supported by the Natural Sciences and Engineering Research Council of Canada (NSERC) through the grant CRDPJ 527642-18 SNOW (Self-driving Navigation Optimized for Winter).

<sup>1</sup>The authors are with Northern Robotics Laboratory, Université Laval, Québec City, Canada, {vladimir.kubelka, maxime.vaidis, francois.pomerleau}@norlab.ulaval.ca

SLAM front-end solutions relying on lidars typically build an incremental 3D map of the environment by registering a current scan using a variant of the original Iterative Closest Point (ICP) algorithm [8]. The ICP algorithm estimates a rigid transformation by iteratively finding corresponding points between two point clouds and minimizing an alignment error. This solution ensures local crisp maps, yet inevitably suffers from global drift [9]. This phenomenon is shown in Figure 1, where a robot navigated autonomously on a 1.5 km path crossing a forest, while only localizing on subsequent scans. This drift problem can be mitigated by SLAM back-ends applying pose graph optimization [1], [10]. Global cues, such as loop closures, are used as constraints to optimize all estimated transformations between the individual lidar scans to ensure global consistency. SLAM back-ends rely on pose-graph optimizers, which require uncertainty estimations in the form of covariance matrices for all transformations. Unfortunately, when it comes to adding constraints produced by ICP, it was shown that, although the uncertainty can be learned or sampled, the Gaussian distribution assumption does not hold up well in complex 3D environments [11].

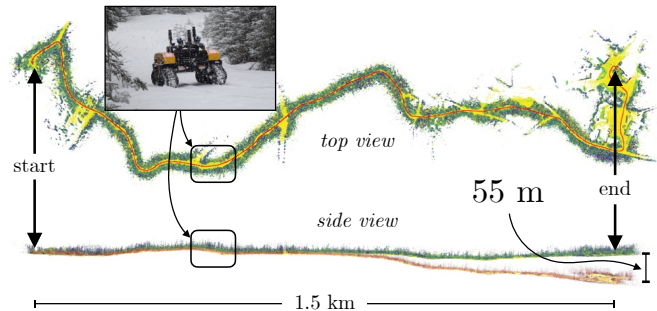


Fig. 1: Example of a drifting localization-based solely on a front-end relying on lidar registration. The top view shows the 3D reconstruction of the forest path over 1.5 km. Color is used to highlight the structure of the environment, with yellow representing the ground. The side view of the same path shows reconstruction drifting by 55 m in elevation with red points and a gravity constrained map in green.

In this paper, we present a tightly-coupled variant of the ICP algorithm, which exploits the directly observable DOFs in the IMU orientation. This way, we obtain pose estimates aligned with the gravity vector. The proposed modification is intended as a lidar SLAM front-end that limits mapping drift. We believe that this front-end has the potential to support the loop closure identification, thus

speeding up convergences of global map optimizations. Our solution has been extensively tested in large-scale outdoor environments as well as in the Defense Advanced Research Projects Agency (DARPA) Subterranean Challenge (SubT).<sup>1</sup> Moreover, the code is readily available to the community as a part of the `libpointmatcher` library.<sup>2</sup>

The remainder of the paper is structured as follows: **Section II** provides a brief overview of the SLAM algorithms that benefit from the IMU modality. **Section III** introduces the modified 4-DOF ICP algorithm including the derivation of the internal optimization step. The following **Section IV** presents our experimental setup and **Section V** discusses the experiment results. Finally, **Section VI** summarizes our findings and concludes the paper.

## II. RELATED WORK

In this section, we first briefly present the visual-inertial SLAM and odometry solutions. Then, the lidar-based systems follow. We divide them into two subgroups according to the manner the IMU modality is exploited. The first subgroup consists of solutions that pre-integrate inertial data into pose increments and use them as penalties in state estimation. The second subgroup is specific by exploiting the gravity force vector that serves as an additional global attitude measurement. Finally, we put our topic, lidar registration, in context with these works.

In the field of visual odometry, the works of Kelly *et al.* [12] and Jones *et al.* [13] presented filtering methods for motion estimation from monocular camera supported by inertial measurements. Besides pose estimation, the algorithms allowed online self-calibration of the camera and IMU coordinate frames. The following extensive research in the field gradually evolved towards graph-based optimization methods, which became computationally feasible thanks to incremental smoothing [14]. To include inertial information into the factor graphs, Forster *et al.* [2] improved the IMU preintegration technique, originally proposed by Lupton *et al.* [15]. The preintegration allows condensing high-rate inertial measurements into compact inter-frame motion penalties. These, in turn, allow real-time operation of visual-inertial odometry and SLAM. When the IMU is not subject to a constantly accelerated motion, the sensed gravitational force makes two of the six pose DOF observable. As stated in Zhang *et al.* [3], in a visual-inertial odometry framework, the gravity vector simplifies the problem to a 4-DOF pose estimation. These DOFs are three positions and one rotation around the vertical axis in a gravity-aligned global reference frame. In our work, we leverage these observations and propose a solution to include this very principle in the lidar-scan-matching process instead of camera-based frameworks.

In the field of lidar SLAM, the IMU modality has attracted attention as well. Shan *et al.* [4] tightly integrated IMU, lidar and Global Positioning System (GPS) in a factor graph optimized by the iSAM2 [14] algorithm. The GPS

and the ability to identify loop closures lead to globally consistent metric maps. A lightweight lidar-inertial ego-motion estimator was presented by Qin *et al.* [16]. They used an iterated error-state Kalman filter to achieve real-time performance, while still gaining from the benefits of tight integration of the sensory data. Similarly, a solution for an Unmanned Aerial Vehicle (UAV) that integrated lidar, IMU and ultra-wide-band ranging modalities was proposed by Nguyen *et al.* [17]. Each modality provided penalties for a sliding-window optimization carried out by the Ceres solver.<sup>3</sup> We see that these works treat the pre-integrated IMU pose increments as penalties in the state estimation process. Closer to our application, Palieri *et al.* [18] introduced their lidar odometry system used in the DARPA SubT Challenge. The IMU modality is integrated more loosely, but it is important for removing motion distortion from lidar scans. They also stressed the necessity of robust operation in harsh conditions and their design dynamically handles sensor modality failures.

Representing the second subgroup, the following works explicitly use the gravity force measurement for stabilizing the vertical orientation of their world coordinate frame and thus their map representation. Zlot *et al.* [5] proposed a lidar mapping solution for underground mines. Apart from benefiting from the inertial measurements as a prior for matching point clouds, they explicitly used gravity vector constraints to ensure the vertical orientation. The gravity vector is one of several linear constraints in their optimization process that smooths prior trajectory. In a tightly integrated lidar-inertial SLAM system for autonomous vehicles, Ye *et al.* [6] used rotation constraints in the global optimization step. The team COSTAR from the SubT competition added explicit gravity factors in their graph representation used in global optimization [7]. In our work, we benefit from the two observable orientation DOFs that also rise from the gravity measurement.

Our solution focuses on the front-end of SLAM systems relying principally on lidar (i.e., on the point-cloud registration). The ICP algorithm iteratively finds corresponding points between two point clouds and looks for a rigid transformation minimizing the alignment error. ICP ensures local consistency, yet inevitably suffers from global drift [9]. This drift can be mitigated by SLAM techniques of global map optimization based on spatial (e.g., loop closures) and measurement constraints (e.g., GPS measurements) [1]. We propose to modify directly the ICP minimization process to exploit observable DOFs from the gravity vector. This leads to searching for pose estimates in a 4-DOF space while limiting the vertical and axial drifts of the local pose estimates.

## III. THEORY

This section first provides a high-level overview of the mapping framework that we use to evaluate the proposed

<sup>1</sup><https://www.darpa.mil/program/darpa-subterranean-challenge>

<sup>2</sup><https://github.com/ethz-asl/libpointmatcher>

<sup>3</sup><http://ceres-solver.org>

ICP modification. Then, it derives the 4-DOF minimization equations for ICP itself.

### A. ICP Mapper

The mapping and subsequent localization are achieved using the freely available `norlab_icp_mapper`.<sup>4</sup> The mapper is lightweight and essentially wraps the ICP functionality while performing input lidar data filtering and memory management for the point cloud map. No global optimization is performed in our setting, the point cloud map grows incrementally as the robot navigates through the environment. The mapper performs the following steps:

- 1) Transform the input lidar scan into the world frame according to the initial pose estimate  $\check{\mathbf{T}}$
- 2) Register the scan with the map using the ICP
- 3) Insert the scan inside the map

The initial estimate  $\check{\mathbf{T}}$  is composed of a translation vector based on the robot odometry and of an orientation quaternion based on the IMU. The input lidar scans are randomly sub-sampled to maintain real-time performance on mobile robots. The input scans are also corrected for the motion distortion according to the odometry and IMU data. Finally, only a subset of the aligned scan points is merged into the map to keep its density bounded.

### B. 4-DOF ICP

The ICP algorithm aims at estimating a rigid transformation  $\hat{\mathbf{T}}$  that best aligns a set of 3D points  $\mathcal{Q}$  (i.e., a *map* point cloud) with a second set of 3D points  $\mathcal{P}$  (i.e., *scan* point cloud), by minimizing the error function  $e$ :

$$\hat{\mathbf{T}} = \arg \min_{\mathbf{T}} e(\mathcal{Q}, \mathcal{P}). \quad (1)$$

In our approach, we choose the *point-to-plane* definition of  $e$  [19] since it outperforms the *point-to-point* definition in most cases [9]. However, the 4-DOF modification can be implicitly extended to the *point-to-Gaussian* error definition since the latter can be translated to the *point-to-plane* as shown by Babin *et al.* [20]. We first define our transformation parameter  $\mathbf{T}$  as a 4D vector  $\boldsymbol{\tau}$ :

$$\boldsymbol{\tau} = \begin{bmatrix} \gamma \\ \mathbf{t} \end{bmatrix} = \begin{bmatrix} \gamma \\ t_x \\ t_y \\ t_z \end{bmatrix}, \quad (2)$$

where  $\gamma$  is the rotational component along the  $\mathbf{z}$  axis, and  $t_x$ ,  $t_y$  and  $t_z$  are the translation components. Compared to the classical 6-DOF definition of  $e$ , please note that  $\boldsymbol{\tau}$  misses the rotational components along the  $\mathbf{x}$  and  $\mathbf{y}$  axes. We then follow with the standard definition of the point-to-plane error function

$$e = \sum_{k=1}^K \left\| [(\mathbf{R}\mathbf{p}_k + \mathbf{t}) - \mathbf{q}_k] \cdot \mathbf{n}_k \right\|_2, \quad (3)$$

<sup>4</sup>[https://github.com/norlab-ulaval/norlab\\_icp\\_mapper](https://github.com/norlab-ulaval/norlab_icp_mapper)

where  $\mathbf{n}_k$  is the normal vector representing the surface at the point  $\mathbf{q}_k$ ,  $\mathbf{R} = R(\gamma)$  is a rotation matrix and the index  $k$  represents paired points from  $\mathcal{Q}$  and  $\mathcal{P}$ . Closely following the minimization derivation from Pomerleau *et al.* [21], yet modified for 4-DOF, the rotation matrix  $\mathbf{R}$  performs only the yaw rotation. The other two rotations are not necessary since the  $\mathcal{P}$  point cloud had already been pre-aligned by the mapper according to the initial  $\check{\mathbf{T}}$  pose estimate. The minimization method relies on rotation matrix linearization. This linearization can be achieved using the small-angle approximation:

$$\mathbf{R} = R(\gamma) \approx \underbrace{\begin{bmatrix} 0 & -1 & 0 \\ 1 & 0 & 0 \\ 0 & 0 & 0 \end{bmatrix}}_{\boldsymbol{\Gamma}} \gamma + \mathbf{I}, \quad (4)$$

where  $\mathbf{I}$  is a unit matrix. In the context of ICP, the impact of linearization is reduced through the iterative process of the whole registration algorithm. Combining (3) with (4), we can approximate the objective function as

$$\begin{aligned} e &\approx \sum_{k=1}^K \left\| [(\boldsymbol{\Gamma}\gamma + \mathbf{I})\mathbf{p}_k + \mathbf{t} - \mathbf{q}_k] \cdot \mathbf{n}_k \right\|_2 \\ &\approx \sum_{k=1}^K \left\| \gamma(\boldsymbol{\Gamma}\mathbf{p}_k) \cdot \mathbf{n}_k + \mathbf{p}_k \cdot \mathbf{n}_k + \mathbf{t} \cdot \mathbf{n}_k - \mathbf{q}_k \cdot \mathbf{n}_k \right\|_2, \end{aligned}$$

which can be rewritten using the *scalar triple product* and by reorganizing the terms, such that

$$\begin{aligned} e &\approx \sum_{k=1}^K \left\| \gamma \underbrace{(\boldsymbol{\Gamma}\mathbf{p}_k) \cdot \mathbf{n}_k}_{\zeta_k} + \mathbf{t} \cdot \mathbf{n}_k - \underbrace{(\mathbf{q}_k - \mathbf{p}_k) \cdot \mathbf{n}_k}_{\mathbf{d}_k} \right\|_2 \\ &\approx \sum_{k=1}^K \left\| \gamma \zeta_k + \mathbf{t} \cdot \mathbf{n}_k - \mathbf{d}_k \cdot \mathbf{n}_k \right\|_2. \end{aligned}$$

We can then minimize the error  $e$  with respect to  $\mathbf{r}$  and  $\mathbf{t}$  and setting the partial derivatives to zero

$$\begin{aligned} \frac{\partial e}{\partial \gamma} &= \sum_{k=1}^K 2\zeta_k(\gamma \zeta_k + \mathbf{t} \cdot \mathbf{n}_k - \mathbf{d}_k \cdot \mathbf{n}_k) = \mathbf{0} \\ \frac{\partial e}{\partial \mathbf{t}} &= \sum_{k=1}^K 2\mathbf{n}_k(\gamma \zeta_k + \mathbf{t} \cdot \mathbf{n}_k - \mathbf{d}_k \cdot \mathbf{n}_k) = \mathbf{0}. \end{aligned}$$

We can assemble these derivatives under the linear form  $\mathbf{A}\boldsymbol{\tau} = \mathbf{b}$ , by bringing the independent variables on the right side of the equation

$$\begin{aligned} \sum_{k=1}^K \begin{bmatrix} \zeta_k(\gamma \zeta_k) + \zeta_k(\mathbf{t} \cdot \mathbf{n}_k) \\ \mathbf{n}_k(\gamma \zeta_k) + \mathbf{n}_k(\mathbf{t} \cdot \mathbf{n}_k) \end{bmatrix} &= \sum_{k=1}^K \begin{bmatrix} \zeta_k(\mathbf{d}_k \cdot \mathbf{n}_k) \\ \mathbf{n}_k(\mathbf{d}_k \cdot \mathbf{n}_k) \end{bmatrix} \\ \sum_{k=1}^K \begin{bmatrix} \zeta_k^2 \gamma + \zeta_k \mathbf{n}_k^\top \mathbf{t} \\ \mathbf{n}_k \zeta_k \gamma + \mathbf{n}_k \mathbf{n}_k^\top \mathbf{t} \end{bmatrix} &= \sum_{k=1}^K \begin{bmatrix} \zeta_k(\mathbf{d}_k \cdot \mathbf{n}_k) \\ \mathbf{n}_k(\mathbf{d}_k \cdot \mathbf{n}_k) \end{bmatrix} \\ \sum_{k=1}^K \begin{bmatrix} \zeta_k^2 & \zeta_k \mathbf{n}_k^\top \\ \zeta_k \mathbf{n}_k & \mathbf{n}_k \mathbf{n}_k^\top \end{bmatrix} \begin{bmatrix} \gamma \\ \mathbf{t} \end{bmatrix} &= \sum_{k=1}^K \begin{bmatrix} \zeta_k \\ \mathbf{n}_k \end{bmatrix} (\mathbf{d}_k \cdot \mathbf{n}_k), \end{aligned}$$

which brings us to the linear system of equations

$$\underbrace{\sum_{k=1}^K \begin{bmatrix} \zeta_k \\ \mathbf{n}_k \end{bmatrix}}_{\mathbf{A}_{4 \times 4}} \underbrace{\begin{bmatrix} \zeta_k & \mathbf{n}_k^\top \end{bmatrix}}_{\mathbf{b}_{4 \times 1}} \boldsymbol{\tau} = \sum_{k=1}^K \underbrace{\begin{bmatrix} \zeta_k \\ \mathbf{n}_k \end{bmatrix}}_{\mathbf{b}_{4 \times 1}} (\mathbf{d}_k \cdot \mathbf{n}_k). \quad (5)$$

Once the matrix  $\mathbf{A}$  and the vector  $\mathbf{b}$  can be constructed, the linear system of Equation (5) can be resolved for  $\boldsymbol{\tau}$  using the Cholesky decomposition. Implementing such solution will require a loop for the summations over  $K$  to build  $\mathbf{A}$  and  $\mathbf{b}$ . An alternative formulation relying on dense matrix multiplication can be computed by assembling

$$\mathbf{G} = \underbrace{\begin{bmatrix} \dots & (\boldsymbol{\Gamma} \mathbf{p}_k) \cdot \mathbf{n}_k & \dots \\ & \mathbf{n}_k & \end{bmatrix}}_{4 \times K}, \quad \mathbf{h} = \underbrace{\begin{bmatrix} \vdots \\ (\mathbf{q}_k - \mathbf{p}_k) \cdot \mathbf{n}_k \\ \vdots \end{bmatrix}}_{K \times 1},$$

leading to

$$\mathbf{A} \boldsymbol{\tau} = \mathbf{b} \Leftrightarrow \mathbf{G} \mathbf{G}^\top \boldsymbol{\tau} = \mathbf{G} \mathbf{h}, \quad (6)$$

which is the final form we use in our implementation. The ICP algorithm iteratively adjusts  $\boldsymbol{\tau}$  according to (6) until the convergence of  $e$ , which indicates the best achievable alignment. Since our definition of  $\boldsymbol{\tau}$  does not involve the rotations in the  $\mathbf{x}$ - $\mathbf{y}$  plane, the resulting alignment and consequently the estimated pose follows the initial IMU values (i.e., the roll and pitch angles remain the same.)

#### IV. EXPERIMENTS

Firstly, the 4-DOF point-to-plane minimizer is readily available in the `libpointmatcher` library under the `force4DOF` option and can be tested with the `norlab_icp_mapper`.<sup>5</sup>

In this section, we present two sets of experiments that demonstrate the performance of the 4-DOF ICP variant and the following Section V then discusses the achieved results. The first set of experiments consists of two runs recorded during the post-event testing session at the DARPA SubT finals (see Figure 3). The second set of experiments covers a 1.5 km long forest trail in the Montmorency research forest.<sup>6</sup> A large tracked robot repeated this path five times in both directions during several days in March 2021.

##### A. DARPA SubT underground environment

Our laboratory, as a member of the CTU-CRAS-NORLAB team, deployed the 4-DOF ICP variant in the Urban circuit and during the competition finals. Its necessity became apparent after the first Mine circuit, where the mapping and localization drifted in a long entrance tunnel. This drift would jeopardize the localization of the scored artifacts in the competition. In this publication, we present two experiments recorded after the competition finals in Kentucky, during the

<sup>5</sup>[https://github.com/norlab-ulaval/norlab\\_icp\\_mapper](https://github.com/norlab-ulaval/norlab_icp_mapper)

<sup>6</sup><https://www.foretmontmorency.ca/en/>

post-event testing. The robot shown in Figure 2 was driven through the underground environment in two separate runs, once through the Urban section (green trajectory in Figure 3) and then through the Mine and Cave sections (purple trajectory). We recorded all sensory data and we are thus able to compare the ICP variants offline. Nevertheless, the mapper performs the same way when launched directly on the robot in real-time. Furthermore, the competition organizers provide a precise, point-cloud map of the environment. It allows us to compute ground-truth reference poses with uncertainty comparable to the lidar sensor noise. For this purpose, we initialize the mapper with the reference map and disable the mapping functionality, thus letting the mapper localize within the reference map.



Fig. 2: The tracked robot driving through the Mine underground environment. It is equipped with an Ouster OS0 128-beam lidar and an Xsens MTI-30 IMU.

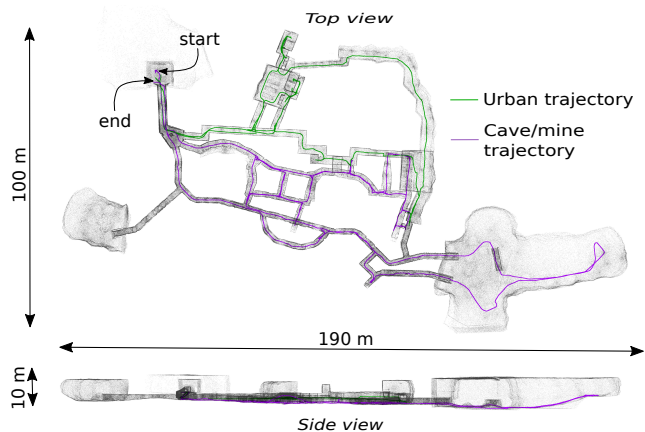


Fig. 3: The underground environment of the final SubT round. The green and violet trajectories denote the *Urban* and *Mine/Cave* experiments recorded during the post-event testing.

##### B. Montmorency forest large-scale outdoor environment

During the winter season of 2021, we deployed a large tracked Clearpath Warthog robot (Figure 4) in the research forest. The purpose of this expedition was the development and testing of a Teach&Repeat functionality for autonomous outdoor navigation (the detailed report [22] is in a review





Fig. 4: The Clearpath Warthog tracked robot. The navigation is based on the front 32-beam RS-LiDAR-32, Xsens MTI-100 IMU and wheel odometry. The robot is also equipped with two Emlid Reach RS+ RTK-GPS receivers used for reference positioning. The other installed sensors were not used for the experiment.



Fig. 5: The 1.5km forest trail in the Montmorency forest autonomously navigated in both directions. The map was adapted from ©Google Earth.

process at the moment). From the data recorded there, we choose a 1.5km forest trail to demonstrate the impact of our approach to mapping and localization in the large-scale outdoor environment of a sub-arctic forest. The robot passed the trail shown in Figure 5 five times in separate experiments during three days. We tested both directions and the weather conditions varied between sub-zero snowy weather and above-zero rain, therefore altering the character of the snow cover. Thanks to accurate reference positioning by RTK-GPS receivers on the robot, we can provide the ground truth positioning and thus evaluate the localization error.

## V. RESULTS

We evaluate the effect of the 4-DOF ICP on localization accuracy by comparing the mapper output with the available ground truth. The metric we choose is the Absolute Trajectory Error (ATE) following Sturm *et al.* [23]. We show its  $z$  component and also its modulus.

### A. DARPA SubT underground environment

Our general experience from the underground environment is that it is well suited for the point-to-plane ICP error function. In the case of the Mine and Cave experiment, the maximum ATE reaches only three to four meters on a trajectory 950 m long, depending on the 4-DOF or classical 6-DOF ICP choice (Figure 6). The shorter Urban experiment performs similarly well, less than one meter in 450 m (Figure 7). We attribute this to the modern 360-degree lidars and plentiful surfaces in this particular underground environment. Also, the course did not contain long uniform tunnels, which are challenging for this type of SLAM. Nevertheless, we observe a trend when switching between 6-DOF and 4-DOF localization: the drift in the  $z$  coordinate is suppressed in both experiments, see Figure 6 and Figure 7. Both approaches drift on the  $x$ - $y$  plane, but this is expected since the IMU does not add any constraints in this plane. In the Mine

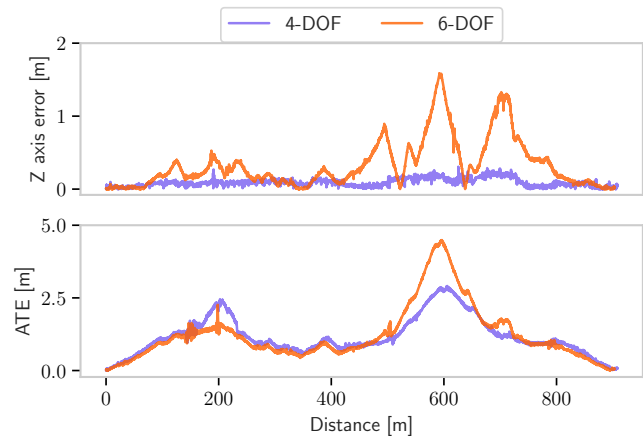


Fig. 6: Comparison of the 4-DOF and 6-DOF ATE during the Mine and Cave experiment in the underground environment. The 4-DOF suppresses the vertical drift (top) which improves the overall ATE (bottom).

and Cave experiment, the ATE of the 4-DOF variant (see Figure 6) momentarily overshoots the 6-DOF error at around 200 m distance due to drift in the  $x$ - $y$  plane, but drift in  $z$  eventually dominates when the robot reaches the edge of the competition course. In the Urban experiment, the  $z$  drift is the dominant contributor to ATE along the whole trajectory and thus the 4-DOF variant helps by suppressing it below 25 cm in the worst case. In both experiments, the ATE drops back to zero as the robot returns to the starting point.

### B. Montmorency forest large-scale outdoor environment

Figure 1 demonstrates the difference between the 4-DOF represented with a green map and the 6-DOF represented in red. Towards the end of the 1.5 km trail, the elevation error can reach 55 m. Unconstrained, the map drifts mainly in the narrow forest corridors, possibly due to the fuzzy vegetation geometry. Incorporating the gravity information in the case of the 4-DOF ICP suppresses this effect. Figure 8 assembles all five runs in one plot, each run with its unique line style.

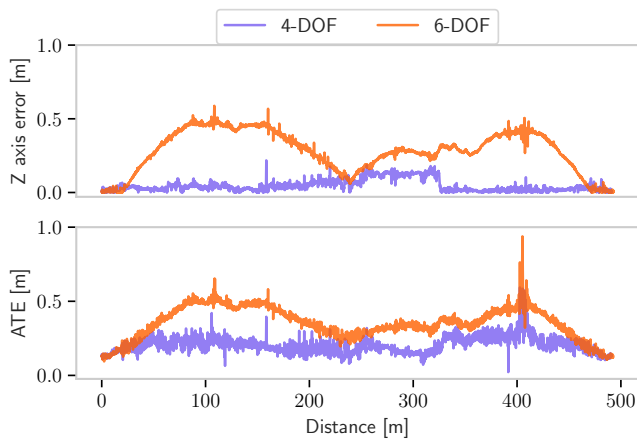


Fig. 7: ATE in the Urban part of the underground environment. The vertical drift was the dominant contributor to ATE in this experiment.

Although the error differs between each run and two runs went in the opposite direction, the trend is clear. Both 4-DOF and 6-DOF drift in the  $x$ - $y$  plane, but the 4-DOF always limits the  $z$  drift. This translates to the total ATE shown in Figure 8 with the slower 4-DOF localization error growth compared to the counterparts in 6-DOF.

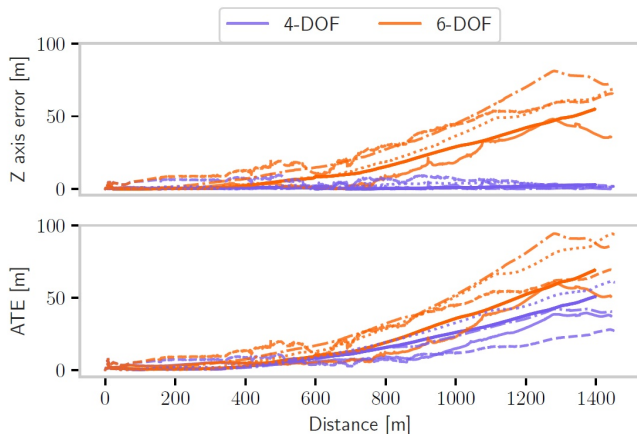


Fig. 8: ATE of the Montmorency forest experiments. Five runs shown together, each with its unique line style. The effect of 4-DOF is evident in the Z axis error.

### C. Normalized ATE analysis

To examine what is the expected localization drift with 4-DOF and the standard 6-DOF ICP variants, we have assembled ATE from all poses and experiments and normalized it by the distance traveled. Figure 9 shows the resulting distributions. 4-DOF limits the median value from 1.48% to 1.05% and also the upper half of the distribution gets compressed with the new third quartile 2.29% instead of 4.19%. This result shows that we cannot eliminate the drift, but we can significantly reduce it by exploiting the IMU

modality, which is usually available on robotic platforms anyway.

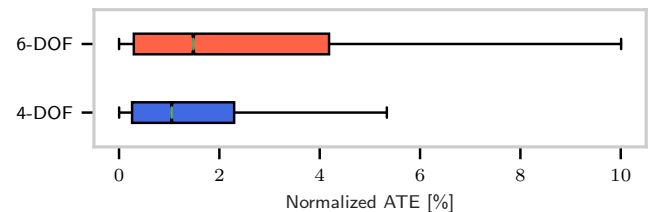


Fig. 9: Normalized ATE of the 4-DOF and 6-DOF variants over all poses and experiments. The first quartile, median and third quartile values are (0.26|1.05|2.29)% and (0.3|1.48|4.19)%, respectively. The black whiskers extend to datapoints in the 1.5x inter-quartile range.

### D. Practical considerations

The presented benefits of the 4-DOF modification are conditioned by correctly estimated roll and pitch angles, and by precise IMU-lidar coordinate frame calibration. In our experiments, we use the Xsens MTI-30 and MTI-100 IMUs which provide sub-degree orientation accuracy in the roll and pitch angles. More importantly, imprecise alignment between the IMU and lidar frames can lead to worse drift than with the classical 6-DOF localization. Our practical approach to the calibration is to use a sufficiently large, flat floor and to adjust the transformation between the sensor frames until the captured point cloud appears flat when transformed to the inertial coordinate frame. The calibration can be further fine-tuned by performing a mapping run in a sufficiently large loop (i.e., more than 500 m) and observing the resulting elevation mismatch. The tangent between the loop length and the error elevation is the final correction of the lidar coordinate frame pitch angle in the inertial frame. This correction can be as low as  $0.1^\circ$  and is sufficient to achieve the results presented in this paper.

## VI. CONCLUSION

In this paper, we have proposed a tightly-coupled variant of the ICP algorithm, which exploits directly observable DOFs in the IMU orientation. It reduces the median normalized ATE by 30% compared to the standard 6-DOF ICP by limiting the vertical drift. The method requires accurate IMU orientation estimates and IMU-lidar calibration. This condition is however achievable with standard sensors and tools. Moreover, the code is readily available to the community as a part of the `libpointmatcher` library. We believe it can be useful as a module in complex graph-based SLAM systems as well as a lightweight lidar odometry with reduced vertical drift.

The 4-DOF ICP has been derived for the point-to-plane error function and implicitly supports the point-to-gaussian error function. Yet, the family of ICP variants is vast and it is for future work to extend this idea to more of them. Moreover, it would be practical to replace the manual IMU-lidar

calibration be an automatic one based on additional external measurements, such as GPS or global map optimization.

#### ACKNOWLEDGMENT

The trajectory analysis in this paper was done using Python package for the evaluation of odometry and SLAM available at <https://github.com/MichaelGrupp/evo>.

#### REFERENCES

- [1] C. Cadena, L. Carlone, H. Carrillo, Y. Latif, D. Scaramuzza, J. Neira, I. Reid, and J. J. Leonard, “Past, present, and future of simultaneous localization and mapping: Toward the robust-perception age,” *IEEE Transactions on Robotics*, vol. 32, pp. 1309–1332, 6 Dec. 2016.
- [2] C. Forster, L. Carlone, F. Dellaert, and D. Scaramuzza, “On-manifold preintegration for real-time visual-inertial odometry,” *IEEE Transactions on Robotics*, vol. 33, 1 2017.
- [3] Z. Zhang, G. Gallego, and D. Scaramuzza, “On the comparison of gauge freedom handling in optimization-based visual-inertial state estimation,” *IEEE Robotics and Automation Letters*, vol. 3, 3 2018.
- [4] T. Shan, B. Englot, D. Meyers, W. Wang, C. Ratti, and D. Rus, “LIO-SAM: Tightly-coupled lidar inertial odometry via smoothing and mapping,” in *IEEE International Conference on Intelligent Robots and Systems*, 2020.
- [5] R. Zlot and M. Bosse, “Efficient large-scale three-dimensional mobile mapping for underground mines,” *Journal of Field Robotics*, vol. 31, pp. 758–779, 5 Sep. 2014.
- [6] H. Ye, Y. Chen, and M. Liu, “Tightly coupled 3d lidar inertial odometry and mapping,” in *IEEE International Conference on Robotics and Automation*, vol. 2019-May, 2019.
- [7] A. Agha, K. Otsu, B. Morrell, *et al.*, *Nebula: Quest for robotic autonomy in challenging environments; team costar at the darpa subterranean challenge*, arXiv preprint arXiv:2103.11470, 2021.
- [8] P. J. Besl and N. D. McKay, “A method for registration of 3-D shapes,” *TPAMI*, vol. 14, no. 2, pp. 239–256, 1992.
- [9] F. Pomerleau, F. Colas, R. Siegwart, and S. Magnenat, “Comparing ICP variants on real-world data sets: Open-source library and experimental protocol,” *Autonomous Robots*, vol. 34, no. 3, pp. 133–148, 2013.
- [10] S. Thrun and M. Montemerlo, “The GraphSLAM Algorithm with Applications to Large-Scale Mapping of Urban Structures,” *IJRR*, vol. 25, no. 5-6, pp. 403–429, 2006.
- [11] D. Landry, F. Pomerleau, and P. Giguère, “CELLO-3D: Estimating the covariance of icp in the real world,” in *2019 International Conference on Robotics and Automation (ICRA)*, 2019, pp. 8190–8196.
- [12] J. Kelly and G. S. Sukhatme, “Visual-inertial sensor fusion: Localization, mapping and sensor-to-sensor self-calibration,” *International Journal of Robotics Research*, vol. 30, 1 2011.
- [13] E. S. Jones and S. Soatto, “Visual-inertial navigation, mapping and localization: A scalable real-time causal approach,” *International Journal of Robotics Research*, vol. 30, 4 2011.
- [14] M. Kaess, H. Johannsson, R. Roberts, V. Ila, J. Leonard, and F. Dellaert, “Isam2: Incremental smoothing and mapping with fluid relinearization and incremental variable reordering,” in *2011 IEEE International Conference on Robotics and Automation*, IEEE, May 2011, pp. 3281–3288.
- [15] T. Lupton and S. Sukkarieh, “Visual-inertial-aided navigation for high-dynamic motion in built environments without initial conditions,” *IEEE Transactions on Robotics*, vol. 28, 1 2012.
- [16] C. Qin, H. Ye, C. E. Pranata, J. Han, S. Zhang, and M. Liu, “LINS: A lidar-inertial state estimator for robust and efficient navigation,” in *IEEE International Conference on Robotics and Automation*, 2020.
- [17] T.-M. Nguyen, M. Cao, S. Yuan, Y. Lyu, T. H. Nguyen, and L. Xie, “Liro: Tightly coupled lidar-inertia-ranging odometry,” in *2021 IEEE International Conference on Robotics and Automation (ICRA)*, 2021, pp. 14 484–14 490.
- [18] M. Palieri, B. Morrell, A. Thakur, *et al.*, “Locus: A multi-sensor lidar-centric solution for high-precision odometry and 3d mapping in real-time,” *IEEE Robotics and Automation Letters*, vol. 6, 2 2021.
- [19] Y. Chen and G. Medioni, “Object modelling by registration of multiple range images,” *Image and Vision Computing*, vol. 10, no. 3, pp. 145–155, 1992, Range Image Understanding.
- [20] P. Babin, P. Dandurand, V. Kubelka, P. Giguère, and F. Pomerleau, “Large-scale 3D mapping of subarctic forests,” in *Proceedings of the Conference on Field and Service Robotics (FSR)*. Springer Tracts in Advanced Robotics, 2019.
- [21] F. Pomerleau, F. Colas, and R. Siegwart, “A review of point cloud registration algorithms for mobile robotics,” *Foundations and Trends in Robotics*, vol. 4, no. 1, pp. 1–104, 2015.
- [22] D. Baril, S. Deschênes, O. Gamache, M. Vaidis, D. LaRocque, J. Laconte, V. Kubelka, P. Giguère, and F. Pomerleau, *Kilometer-scale autonomous navigation in subarctic forests: Challenges and lessons learned*, arXiv preprint arXiv:2111.13981, 2021.
- [23] J. Sturm, N. Engelhard, F. Endres, W. Burgard, and D. Cremers, “A benchmark for the evaluation of RGB-D SLAM systems,” in *IEEE International Conference on Intelligent Robots and Systems*, 2012.